phenomena, such as debris flows formed by melting of near-surface ground ice, were possible. In practice, such debris flows may have only occurred in some favored areas, because a relatively large amount of water is required in combination with the presence of cohesionless material (in East Greenland, debris flows are not generalized but only occur where large amount of debris is produced). Nevertheless, the possible presence of limited amounts of liquid water in the near surface at mid- and high latitudes predicted by our model have interesting consequences. It could induce freeze-thaw cycle erosion on Mars, and explain the polygons and patterned ground observed on MOC images (*8*) around 60° latitude, which look similar to terrestrial polygons related to the seasonal thawing of ground.

References and Notes

1. M. C. Malin, K. E. Edgett, *Science* **288**, 2330 (2000).
2. D. S. Musselwhite, T. D. Swindle, J. I. Lunine, *Geophys. Res. Lett.* **28**, 1283 (2001).
3. L. P. Knauth, S. Klonowski, D. Burt, *Science* **290**, 711 (2000).
4. However, we did find some alcoves and gullies covered by dust and a few impacts that could correspond to older debris flows. See, for example, MOC images M00-00530 and M03-01969.
5. W. K. Hartman, *Space Sci. Rev.* **96**, 405 (2001).
6. M. T. Mellon, R. J. Phillips, *Lunar Planet. Sci. Conf.* **32**, abstract no. 1182 (2001).
7. E. J. Gaidos, *Icarus* **153**, 218 (2001).
8. V. R. Baker, *Nature* **412**, 228 (2001).
9. A. M. Johnson, J. R. Rodine, in *Slope Instability*, D. Brundsen, D. B. Prior, Eds. (Wiley, New York, 1984).
10. Debris flows in East Greenland were observed by two of us during two field trips in July 1987 and August 1989. Jameson Land (70°N) is located north of the Scoresby Sund fjord and comprises wide plateaus 600 to 1000 m high mainly composed of clastic sediments (Permian to Lower Cretaceous age).
11. J. P. Peulvast, *Geogr. Ann. Ser. A* **70**, 351 (1988).
12. In the dry periglacial environment of Jameson land, direct runoff from rain is not thought to be the main process creating debris flows, although summer rains can contribute to the erosion of the plateau through shallow hortonian gullying on bare slopes. The mean annual precipitation is estimated to be only about 200 to 250 mm, mainly as snowfalls. Also, water springs were not observed where debris flows form.
13. J. L. Innes, *Phys. Geogr.* **7**, 469 (1983).
14. S. A. Harris, C. A. Gustafson, *Z. Geomorphol. N.F* **37**, 41 (1993).
15. P. A. Allen, *Earth Surface Processes* (Blackwell Science, Oxford, UK, 1997).
16. Navier-Coulomb law gives $\tau = C + (\sigma - P)\tan\phi$, where τ is the critical shear stress at failure, C the cohesion, σ the normal stress, P the pore fluid pressure, and ϕ the coefficient of internal friction. As the fluid pressure increases, the shear stress decreases and failure may occur. This process is efficient on steep slopes because the dry material is already near the critical shear stress before incorporation of water. Consequently, debris flows usually start at the most elevated point of debris aprons. This may explain the observation that some martian debris flows seem to start at the same level underneath scarps (Fig. 1).
17. J. Touma, J. Wisdom, *Science* **259**, 1294 (1993).
18. J. Laskar, *Celestial Mech.* **64**, 115 (1999).
19. H. H. Kieffer, A. P. Zent, in *Mars*, H. H. Kieffer, B. M. Jakosky, C. W. Snyder, M. S. Matthews, Eds. (Univ. of Arizona Press, Tuscon, AZ, 1992).
20. M. H. Carr, *Icarus* **56**, 47 (1983).
21. T. Z. Martin, A. R. Peterfreund, E. D. Miner, H. H. Kieffer, G. E. Hunt, *J. Geophys. Res.* **84**, 2830 (1979).
22. F. Forget *et al.*, *J. Geophys. Res.* **104**, 24155 (1999).
23. S. R. Lewis *et al.*, *J. Geophys. Res.* **104**, 24177 (1999).
24. To calculate the surface energy balance on a slope, the incident direct solar flux was modified to account for the actual sun incident angle on the slope. The solar flux scattered by the airborne dust was also modified, assuming that 50% of the scattered flux is coming from the direction of the sun and that the other 50% is more isotropic and thus not affected by the orientation of the slope. This assumption is supported by three-dimensional Monte Carlo simulations performed separately, which showed that, for opacity below unity, about 50% of the scattered light typically originates from less than a 15% portion of the sky centered on the sun.
25. The calculation shown here corresponds to the last year of 3.5-year simulations performed with a 30-min time step. We assumed a surface pressure of 700 Pa and a visible dust optical depth $\tau = 0.2$. Surface emissivity, thermal inertia, ground albedo, and CO_2 ice albedo were set to 0.95, 260 SI, 0.2, and 0.5, respectively. In practice, our results were found to be quite insensitive to the variations of these parameters, giving us some confidence in our ability to apply our conclusions to other epochs with different obliquities. The maximum diurnal averaged temperature significantly changes only in the case of large dust opacity (−6 K for $\tau = 1$, −18 K for $\tau = 5$).
26. Web fig. 1 is available at Science *Online* at www.sciencemag.org/cgi/content/full/1066698/DC1.
27. O. B. Toon *et al.*, *Icarus* **44**, 552 (1980).
28. M. I. Richardson, R. J. Wilson, *Bull. Am. Astron. Soc.* **32**, 1092 (2001).
29. M. T. Mellon, B. M. Jakosky, *J. Geophys. Res.* **100**, 11781 (1995).

30. We thank D. Mercier, P. Coussot, and R. M. Haberle for helpful discussions. We acknowledge the use of MOC images processed by Malin Space Science Systems. The Mars climate model has been developed in collaboration with the University of Oxford with the support of CNRS, the European Space Agency [TRP contract 11369/95/NL/JG(SC)], and the Centre National d'Etudes Spatiales. Supported by the Programme National de Planétologie, Institut National des Sciences de l'Univers, CNRS, France.

1 October 2001; accepted 16 November 2001
Published online 29 November 2001;
10.1126/science.1066698
Include this information when citing this paper.

Quantifying Uncertainties in Climate System Properties with the Use of Recent Climate Observations

Chris E. Forest,[1]* Peter H. Stone,[1] Andrei P. Sokolov,[1] Myles R. Allen,[2] Mort D. Webster[1]†

We derive joint probability density distributions for three key uncertain properties of the climate system, using an optimal fingerprinting approach to compare simulations of an intermediate complexity climate model with three distinct diagnostics of recent climate observations. On the basis of the marginal probability distributions, the 5 to 95% confidence intervals are 1.4 to 7.7 kelvin for climate sensitivity and −0.30 to −0.95 watt per square meter for the net aerosol forcing. The oceanic heat uptake is not well constrained, but ocean temperature observations do help to constrain climate sensitivity. The uncertainty in the net aerosol forcing is much smaller than the uncertainty range for the indirect aerosol forcing alone given in the Intergovernmental Panel on Climate Change Third Assessment Report.

Estimation of the uncertainty in long-term climate projections requires estimates of the probability density functions (pdfs) of key properties of the climate system. Attempts thus far (*1*, *2*) have used pdfs based on expert judgment to analyze such uncertainty. For near-term climate change, recent studies (*3*) have applied the uncertainty estimates derived from the climate change detection algorithm for particular models to climate projections based on these models. A key assumption in this approach is that both forcing and response do not change qualitatively between observed and forecast periods. Hence, it is not applicable to modeled climate change under scenarios that differ substantially from the recent past (e.g., stabilization cases or severe changes in sulfur emissions). Given the political priority to establish what constitutes a "safe" stabilization level for greenhouse gases, an objective means of quantifying uncertainty in the long-term response, despite uncertainty in other forcings, is clearly desirable.

These problems can be addressed in large part by determining both the range of climate system properties and the range of forcings that produce simulations consistent with

[1]Joint Program on the Science Policy of Global Change, Massachusetts Institute of Technology, Cambridge, MA 02139, USA. [2]Department of Physics, Oxford University, Oxford, OX1 3PU UK.

*To whom correspondence should be addressed. E-mail: ceforest@mit.edu

†Present address: Department of Public Policy, University of North Carolina, Chapel Hill, NC 27599, USA.

20th-century climate change (*4*, *5*). The two most uncertain properties that control the climate system's decadal to century response to radiative forcings are climate sensitivity (S) and the rate of heat uptake by the deep ocean (K_v) (*6*). Simulations by modern atmosphere-ocean general circulation models (AOGCMs) reveal substantial differences in these properties between models (*5*). Previous estimates of the uncertainties in these quantities have generally been based only on expert judgment and/or on the range of values found in AOGCMs. A recent exception has estimated the range of climate sensitivity from observations but with substantial simplifications compared with this study (*7*, *8*). Although positive AOGCM climate change detection results place a lower bound on climate sensitivity (*3*, *5*), the upper bound on S depends strongly on the rate of ocean heat uptake (*3*, *5*). The Massachusetts Institute of Technology (MIT) climate model has the flexibility to vary both S and K_v, unlike AOGCMs (*9*).

The primary uncertainty in the radiative forcing is the total uncertainty in anthropogenic aerosol forcing that arises from the uncertainty in aerosol radiative properties and cloud effects as well as in their concentrations over the industrial period (*10*, *11*). [Uncertainty in the natural forcings (primarily solar and volcanic forcings) exists although the estimated changes during the 20th century appear to be small compared with the uncertainty in the aerosol forcing (*11*).] Improving on previous results (*4*, *5*), we include the strength of the anthropogenic aerosol forcing as a third uncertainty. We describe this uncertainty by the net forcing (both direct and indirect) for the decade of the 1980s (F_{aer}) relative to pre-1860 levels.

We use the MIT two-dimensional (2D) (zonal mean) statistical-dynamical model (*8*), specifying both S and K_v as well as F_{aer}, to simulate the climate for the 1860–1995 period. We systematically vary the parameters in question to assess which simulations "match" the observed climate record. We make two substantial improvements on previous studies. First, we apply the optimal fingerprint detection algorithm (*12*–*14*) to three independent diagnostics of the recent climate record and to the results of climate simulations, whereas previous results (*4*, *5*, *7*) were based on comparisons with a single climate diagnostic. Second, we derive a joint pdf for the three uncertain properties of the climate system: S, K_v, and F_{aer}, taking into account that the probabilities for each parameter are conditional on the other values, which independent pdfs would not. From this joint pdf, we can then determine the likelihood of the climate system response to individual forcing scenarios (*15*).

The three diagnostics are derived from the upper-air temperature record (*16*), the surface temperature record (*17*, *18*), and the record of ocean temperatures (*19*). As in (*4*, *5*), we use the same upper-air temperature diagnostic as in (*14*, *20*). The temperature changes are computed for points on a latitude-height grid as the difference in the 1986–95 and 1961–80 zonal means. The years 1963–64 and 1992 were removed to limit the effect of the Mount Agung and Mount Pinatubo eruptions on the estimated temperature changes.

We construct a surface temperature diagnostic (Fig. 1A) by computing decadal mean temperature anomalies for the 1946–95 period with respect to a 1906–95 climatology from the surface temperature record of (*17*, *18*). Using an observational data mask, we compute area-weighted zonal averages for the temperature anomalies over four zonal bands (90°S to 30°S, 30°S to 0°, 0° to 30°N, and 30°N to 90°N) and create a latitude-time pattern of temperature change. By using a longer climatology, we make use of the additional information that the most recent 50 years were warmer than the previous 40 [see (*3*, *21*)]. For both the surface and upper-air temperature diagnostics, the observational errors are small on such spatial scales compared with natural variability (*22*) and are neglected in this analysis.

Our third climate change diagnostic is the trend in global-average ocean temperatures down to 3000-m depth (Fig. 1B) computed from estimates in (*19*). We compute a trend from a 44-point time series of 5-year averages using the 1948–95 period. Ordinary least squares regression is used to compute the trend with the observational errors providing uncertainty in the estimated trend. Because the data are sparsely distributed across ocean basins, the global average will have uncertainty because of this sampling error. One attempt to include this is provided (*19*), but the true uncertainty remains unknown. This observational error was then added to the climate noise estimate discussed next.

Each diagnostic is used to compute a goodness-of-fit statistic, r^2, which is inversely weighted by the size of the deviations that we should expect from climate noise (*4*, *5*, *23*). For each diagnostic, the climate noise estimates were taken from successive segments of control simulations of two AOGCMs (*24*). For the ocean diagnostic, an additional estimate of the observational error was included. From the r^2 statistics, a likelihood is computed to provide a joint probability distribution for the model parameter space given the independent observations (*4*, *5*). This likelihood estimate represents the probability that a particular choice of model parameters is correct given the observed record of climate change. More formally, we reject a choice of model parameters, Π ($\Pi = \{S, K_v, F_{aer}\}$), as producing a simulation of the 20th century that is inconsistent with observed climate given the unforced variability of the climate as estimated by AOGCMs (*24*) at some level of significance. The distribution of the r^2 statistic for a given diagnostic indicates the diagnostic's ability to reject particular regions of parameter space (Fig. 2).

In general, the combination of lower oceanic heat uptake, higher climate sensitivity, and weaker aerosol cooling will provide a simulation with a larger change in surface and upper-air temperatures (Fig. 1). For the deep ocean, however, a larger warming will occur for stronger oceanic heat uptake. For low climate sensitivity, these differences in response show little dependence on oceanic heat uptake. Thus, each diagnostic provides distinct constraints on the parameter space. The surface and upper-air diagnostics reject similar regions of parameter space, namely low K_v and high S, whereas the ocean diagnostic shows a rejection of the high K_v and high S region. When aerosol cooling is increased (decreased) (not shown for each diagnostic), the rejection regions shift toward the higher (lower) response regions, indicat-

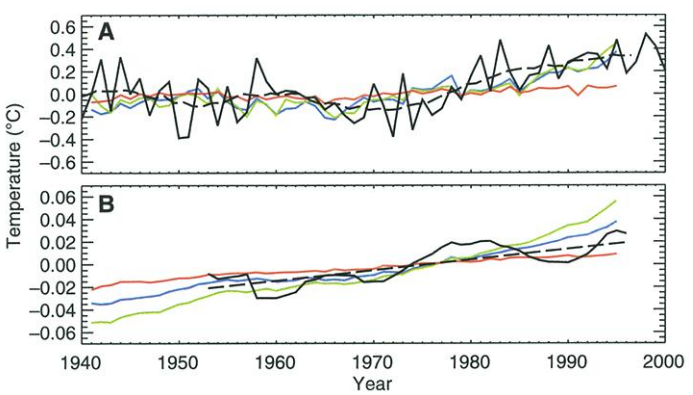

Fig. 1. Global-mean surface (**A**) and deep-ocean temperatures (**B**) for observations (black) and the ensemble averages for three simulations (blue, S = 3.0 K, K_v = 7.5 cm^2/s, F_{aer} = −0.75 W/m^2; green, S = 6.2 K, K_v = 20. cm^2/s, F_{aer} = −0.75 W/m^2; and red, S = 0.4 K, K_v = 2.5 cm^2/s; F_{aer} = −0.75 W/m^2; see Fig. 2). The blue case used model parameters near the median values in Fig. 4. The green case is accepted on the basis of surface temperature data but rejected by deep-ocean temperatures, and vice versa for the red case. The black dashed lines indicate the 10-year running mean (A) and the linear trend (B) estimated from the respective observational data. All temperatures are anomalies from the 1961–90 average.

ing that a higher sensitivity is required to reproduce the observed temperature changes.

Because individual diagnostics provide the likelihood that the modeled temperature change is correct given a set of model parameters [or in Bayesian notation, $p(\Delta T|\Pi)$], we use results from each diagnostic to update the probability distribution $p(\Pi|\Delta T)$ by applying Bayes' theorem (*25*, *26*). By choosing one distribution as the initial prior, two sequential posterior distributions are computed with the final distribution representing the combined uncertainty from the three climate change diagnostics. If desired, a prior distribution based on expert judgment can be used initially. In the absence of an expert prior, we assume a uniform probability distribution as the first prior (*27*).

The combined probability distribution (Fig. 3) resulting from the Bayesian updating procedure indicates that the constraints on climate sensitivity and aerosol forcing are fairly strong, whereas oceanic heat uptake is less constrained. Recent papers (*28*, *29*) have examined the dependence of ocean temperature trends in specific basins, which may provide better constraints. The marginal pdfs (Fig. 4) summarize each parameter's uncertainty by accounting for uncertainty in others (*30*). We also show the result when an expert prior (*31*) is used for climate sensitivity while keeping uniform priors on K_v and F_{aer}. This demonstrates that including expert judgment will alter the marginal pdf for climate sensitivity and changes the pdf(F_{aer}) to compensate for the reduced likelihood of high climate sensitivities. Although expert judgments are in part subjective, they can take into account information not included in our analysis, such as paleoclimate data.

The joint probability distribution for S, K_v, and F_{aer} shows stronger constraints on model properties than earlier results (*4*, *5*, *7*) owing to two improvements in our analysis. Aerosol-forcing uncertainty is now considered explicitly, and the additional diagnostics place limits on previously unconstrained regions of parameter space.

With uniform priors, the strength of the net aerosol forcing lies within −0.3 to −0.95 W/m^2 for the 5 to 95% confidence range. The main diagnostic constraining this forcing is the surface temperature record. We stress that the constrained quantity in this case is the net nongreenhouse gas forcing. This uncertainty range is much smaller than the uncertainty range given by the Intergovernmental Panel on Climate Change (IPCC) (*11*) for the indirect aerosol forcing alone.

For the effective ocean diffusivity, the 5 to 95% confidence range is 1.8 to 56.0 cm^2/s. Although the lower bound is well constrained by the observations (see Fig. 2), the estimated probabilities are affected by the assumed prior. This large uncertainty is much greater

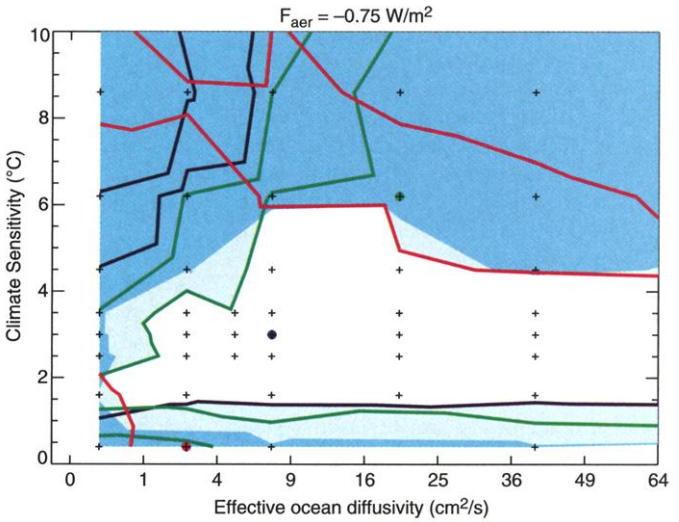

Fig. 2. Composite of the parameter rejection regions estimated by individual diagnostics given a net aerosol forcing of −0.75 W/m^2. The light shaded region would be rejected by at least one climate change diagnostic at the 10% significance level. However, when we combine all three sources of information, then only the dark shaded region is rejected, which illustrates that more than a single diagnostic is required for adequate rejection. The individual rejection region boundaries for upper-air (black), surface-air (green), and deep-ocean temperatures (red) show the effect of each diagnostic on the distribution in Fig. 3D. The rejection boundaries for the 1% significance level are also shown as are the locations of model simulations (+). Circles show the locations for the cases shown in Fig. 1.

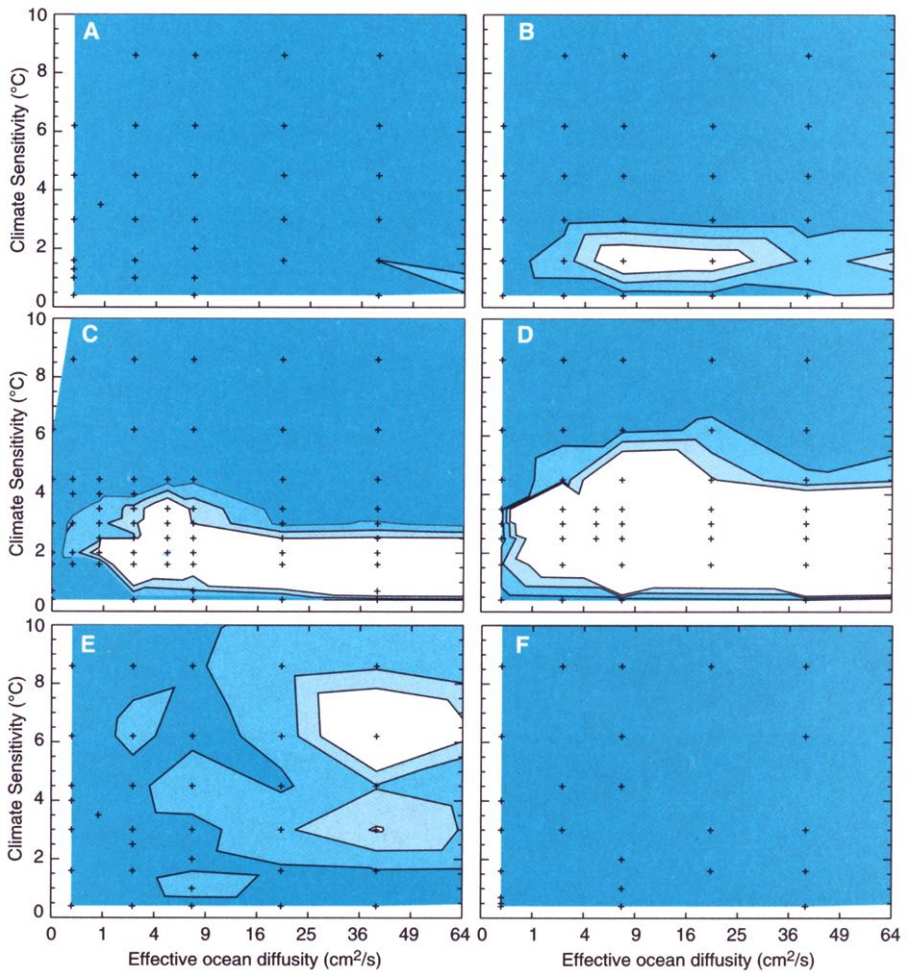

Fig. 3. (**A** to **F**) The dependence of the final updated distribution of r^2 on S and K_v (vertical and horizontal axes) and on net aerosol forcing (F_{aer} = 0.0, −0.25, −0.5, −0.75, −1.0, and −1.5 W/m^2 in A to F, respectively). The thick lines and shading represent the rejection region boundaries at the 20, 10, and 1% levels of significance (from light to dark, respectively). Locations of model simulations are indicated by a plus symbol.

than that usually assumed (*2*, *7*, *32*). Ocean heat uptake remains one of the least understood large-scale processes in climate change studies. Although many mechanisms are known to affect heat uptake in the ocean, the sensitivity of the global heat uptake to changes in model parameterizations for these mechanisms is poorly understood (*33*). Our result suggests that more research is required.

With uniform priors, the 5 to 95% confidence range for the climate sensitivity is estimated to be 1.4 to 7.7 K. We estimate the probability of S being outside the IPCC's range of 1.5 to 4.5 K (*32*) to be 30% with a 23% chance of exceeding 4.5 K. With an expert prior applied to climate sensitivity and uniform priors elsewhere, climate sensitivity is estimated to be within 1.3 to 4.2 K for the 5 to 95% range, and the probability of S being outside the IPCC's range decreases to 12% with a 3.5% chance of exceeding 4.5 K. It is not surprising that the application of the expert prior improves agreement with the IPCC range, because both are based on similar evidence and reasoning.

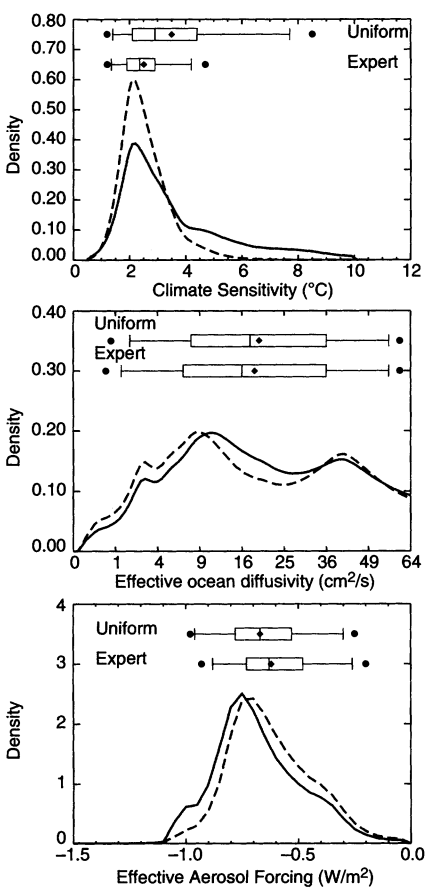

Fig. 4. Marginal pdfs for three climate model parameters with (dashed) and without (solid) the use of an expert prior for climate sensitivity (*31*). The whisker plots show the 2.5 to 97.5% (dots), 5 to 95% (vertical bars on ends), and 25 to 75% (box) probability ranges along with the median (bar within box) and mean (diamond) for each distribution. The main impact of the expert prior is to eliminate the "fat tail" of high sensitivity values that are not excluded on the basis of recent obervations alone.

Although the estimated pdf is consistent with the r^2 distributions, nonzero probabilities will always exist outside the explored parameter region (as indicated by the nonzero probability for climate sensitivity at 10.0 K). We could fit specific theoretical distributions and use these to calculate the probability of the tail regions. For example, a range of theoretical distribution families fit to the climate sensitivity pdf indicate roughly a 3.5% chance that $S > 10$ K. However, these distributions all have infinite tails. Alternatively, we could assume that the probability outside the region explored is negligible.

Our estimates of probability are independent of the MIT 2D model to the extent that this model represents the large-scale behavior of different 3D AOGCMs. On the basis of comparisons of the transient behavior under various forcing scenarios (*9*), the model behavior matches AOGCMs well for 100- to 150-year simulations. The MIT model cannot simulate certain nonlinearities (e.g., the shutdown of the thermohaline circulation), but there is no indication of such behavior over the past 150 years. As was shown in (*9*), the dependence of changes in different characteristics on surface warming for different versions of the MIT model is similar to that for the different AOGCMs. Because we chose to explore ranges of model parameters that extend beyond typical values of properties of existing AOGCMs, it is important to note that the MIT model produces similar dependencies for the range of climate sensitivity used in this study.

As described in the IPCC Third Assessment Report (*11*), a long list of forcings can be identified for the industrial period (1750 to present). We included the three forcings (greenhouse gases, sulfate aerosols, and stratospheric ozone) that we expect to be most important for the diagnostics we used. When considering the implications of the marginal pdf(F_{aer}), we note that neglected forcings, which have patterns similar to those of the sulfate aerosols, are implicitly included. Latitudinal variations dominate this pattern (*11*, *34*), adding further support for our using a zonal mean model. The most serious omission would be a forcing with a unique spatial pattern.

Among the possible forcing factors (*11*), the changes attributed to biomass burning, mineral dust, land-use change, and solar activity particularly have spatial distributions different from sulfate aerosols. These estimated forcings combine to produce a forcing of -0.1 W/m^2. The forcings with patterns similar to sulfate aerosols (tropospheric ozone, sulfate, black carbon, organic carbon, and aerosol indirect effect) total an estimated -0.95 W/m^2. Thus, we doubt that the additional factors would substantially alter our results. Because we use the temperature record for 1906–95, only the forcings for this period should matter.

As discussed previously (*5*), the estimated natural variability, which is used to compute the noise covariance matrix in the detection algorithm, is obtained from two AOGCMs (*24*). Thus, we implicitly neglected the expected dependence of natural variability on climate sensitivity or ocean heat uptake (*35*).

Despite these caveats, the estimated $p(\Pi|\Delta T)$ presented here provides an essential improvement in quantifying uncertainty in future projections of climate change. In particular, the method for estimating pdfs is based on an objective technique and can be updated with subjective information if desired. The distinction between objective and subjective components provides a clearer interpretation of the results that can be used to guide policy-makers engaged in the climate change debate.

References and Notes

1. J. G. Titus, V. Narayanan, *Clim. Change* **33**, 151 (1996).
2. T. M. L. Wigley, S. C. B. Raper, *Science* **293**, 451 (2001).
3. M. R. Allen, P. A. Stott, R. Schnur, T. Delworth, J. F. B. Mitchell, *Nature* **407**, 617 (2000).
4. C. E. Forest, M. R. Allen, P. H. Stone, A. P. Sokolov, *Geophys. Res. Lett.* **27**, 569 (2000).
5. C. E. Forest, M. R. Allen, A. P. Sokolov, P. H. Stone, *Clim. Dyn.*, in press.
6. Here we define climate sensitivity (S) as the equilibrium global-mean surface temperature change in response to a doubling of CO_2 concentration. We measure the rate of heat uptake by the deep ocean by an effective global diffusivity of heat anomalies (K_v) into the ocean below the climatological mixed layer. For AOGCMs, this effective diffusivity can be derived from transient climate change experiments and should not be confused with the model's sub–grid scale diffusion coefficient. S and K_v are closely related to the climate sensitivity and transient climate response factors used in (*36*) to represent both the short- and long-term behavior of AOGCMs.
7. N. G. Andronova, M. E. Schlesinger, *J. Geophys. Res.* **106**, 22605 (2001).
8. This analysis, in contrast to ours, used a simple energy balance model, relied solely on surface temperatures, and did not take into account the uncertain ocean heat uptake.
9. A. P. Sokolov, P. H. Stone, *Clim. Dyn.* **14**, 291 (1998).
10. J. E. Penner *et al.*, in *Climate Change 2001, The Scientific Basis*, J. T. Houghton *et al.*, Eds. (Cambridge Univ. Press, Cambridge, 2001), pp. 289–348.
11. V. Ramaswamy *et al.*, in *Climate Change 2001, The Scientific Basis*, J. T. Houghton *et al.*, Eds. (Cambridge Univ. Press, Cambridge, 2001), pp. 349–416.
12. K. Hasselmann, in *Meteorology of Tropical Oceans*, D. B. Shawn, Ed. (Royal Meteorological Society, Bracknell, UK, 1979), pp. 251–259.
13. T. L. Bell, *J. Geophys. Res.* **87**, 11161 (1982).
14. M. R. Allen, S. F. B. Tett, *Clim. Dyn.* **15**, 419 (1999).
15. M. D. Webster *et al.*, *MIT Joint Program on the Science and Policy of Global Change Report 73* (Massachusetts Institute of Technology, Cambridge, MA, 2001), pp. 1–3.
16. D. E. Parker *et al.*, *Geophys. Res. Lett.* **24**, 1499 (1997).
17. P. D. Jones, *J. Clim.* **7**, 1794 (1994).
18. P. D. Jones, M. New, D. E. Parker, S. Martin, I. G. Rigor, *Rev. Geophys.* **37**, 173 (1999).
19. S. Levitus, J. Antonov, T. P. Boyer, C. Stephens, *Science* **287**, 2225 (2000).
20. S. F. B. Tett, J. F. B. Mitchell, D. E. Parker, M. R. Allen, *Science* **274**, 1170 (1996).

21. M. R. Allen *et al.*, *Surv. Geophys.*, in press.
22. G. C. Hegerl, P. D. Jones, T. P. Barnett, *J. Clim.* **14**, 198 (2001).
23. $r^2 = u^T C_N^{-1} u$, where u is the difference vector between the observation and model data ($y_{obs} - y_{model}$) and C_N^{-1} is the inverse of the climate noise covariance matrix as estimated from segments of AOGCM control simulations. Because only limited length control segments are available, a truncated representation of C_N^{-1} must be used, based on a projection onto the κ leading eigenvectors of the estimated C_N (*21*). We use $\kappa = 14$ for both the surface and upper-air temperature diagnostics, but similar results are obtained for a range of truncations (*5*). As described in (*5*), $\Delta r^2 \sim mF_{m,n}$, where $F_{m,n}$ is the F statistic with m and n degrees of freedom, m is the number of constrained model properties, and n is the degrees of freedom in estimated climate noise. Hence, Δr^2 provides a basis for rejecting climate model simulations as being inconsistent with the simulation with the minimum r^2 value. For a given level of significance, we compute the appropriate F statistic that provides a cutoff value for r^2. If r^2 is above this cutoff value, we reject the hypothesis that the Δr^2 is consistent with estimated climate noise.
24. For the surface and upper-air diagnostics, the climate noise was estimated from the second-generation AOGCM developed at the Hadley Centre for Climate Prediction and Research (HadCM2) (*37*). For the ocean diagnostic, the Geophysical Fluid Dynamics Laboratory AOGCM, GFDL_R30_c (*38*), was used because estimates from HadCM2 were not readily available.
25. T. Bayes, *Philos. Trans. R. Soc.* **53**, 370 (1763).
26. To compute the updated distributions for $p(\Pi|\Delta T)$, we first interpolate the r^2 values onto a finer grid [$\Delta S = 0.1$ K, $\Delta(K_v^{1/2}) = 0.1$ cm/s$^{1/2}$] over the range $S = 0.5$ to 10 K and $K_v = 0.2$ to 64 cm^2/s. After the data were interpolated in the S-K_v plane, we interpolated between the aerosol forcing levels to a resolution of $\Delta F_{aer} = 0.05$ W/m^2 over the range 0 to 1.5 W/m^2. After the r^2 values were interpolated, the probability of rejection was estimated (*23*) to generate the probability distribution on the finer grid. For all integral estimates of total probability or marginal probability distributions, the finer grid spacing was used over the ranges specified.
27. The ranges explored for the model parameters set the limits of the uniform priors: $S = 0.5$ to 10 K, $K_v = 0.2$ to 64 cm^2/s, and $F_{aer} = -1.5$ to 0 W/m^2. We can assess the impact of these priors by examining the posterior distributions.
28. T. P. Barnett, D. W. Pierce, R. Schnur, *Science* **292**, 270 (2001).
29. S. Levitus *et al.*, *Science* **292**, 267 (2001).
30. Marginal pdf(Π_i) $\equiv \int p(\Pi) d\Pi_j$, where Π_i is the ith parameter and $D_{j \neq i}$ is the parameter-space domain not including i.
31. M. D. Webster, A. P. Sokolov, *Clim. Change* **46**, 417 (2000).
32. U. Cubasch *et al.*, in *Climate Change 2001, The Scientific Basis*, J. T. Houghton *et al.*, Eds. (Cambridge Univ. Press, Cambridge, 2001), pp. 525–582.
33. J. M. Gregory, *Clim. Dyn.* **16**, 501 (2000).
34. J. Hansen *et al.*, *J. Geophys. Res.*, in press.
35. T. M. L. Wigley, S. C. B. Raper, *Nature* **344**, 324 (1990).
36. S. C. B. Raper, J. Gregory, R. S. Stouffer, *J. Clim.* **15**, 124 (2002).
37. T. C. Johns *et al.*, *Clim. Dyn.* **13**, 103 (1997).
38. T. R. Knutson, T. L. Delworth, K. W. Dixon, R. J. Stouffer, *J. Geophys. Res.* **104**, 30981 (1999).
39. We thank N. Gillett for streamlining the fingerprint detection code, T. Delworth for GFDL_R30_c ocean data, J. Antonov for deep-ocean temperature data, the Hadley Centre for Climate Prediction and Research for HadCM2 data, and A. Slinn for her graphics expertise. This work was supported by a National Oceanic and Atmospheric Administration Office of Global Programs grant NA06GP0061 (C.E.F.) and the European Commission QUARCC project (M.R.A.). The control run of HadCM2 was funded by the UK Department of the Environment, Transport, and Regions under contract number PECD 7/12/37.

16 July 2001; accepted 14 November 2001

Intracellular Iron Minerals in a Dissimilatory Iron-Reducing Bacterium

Susan Glasauer,* Sean Langley, Terry J. Beveridge

Among prokaryotes, there are few examples of controlled mineral formation; the formation of crystalline iron oxides and sulfides [magnetite (Fe_3O_4) or greigite (Fe_3S_4)] by magnetotactic bacteria is an exception. *Shewanella putrefaciens* CN32, a Gram-negative, facultative anaerobic bacterium that is capable of dissimilatory iron reduction, produced microscopic intracellular grains of iron oxide minerals during growth on two-line ferrihydrite in a hydrogen-argon atmosphere. The minerals, formed at iron concentrations found in the soil and sedimentary environments where these bacteria are active, could represent an unexplored pathway for the cycling of iron by bacteria.

Many of the metabolic pathways affecting mineral-bacterium interactions in anaerobic subsurface environments are poorly defined, despite their potential impact on the lithosphere and hydrosphere. Metal-reducing *Shewanella* spp. are known to use mineral-bound Fe(III) [e.g., Fe (hydr)oxides] as the terminal electron acceptor for the membrane-bound electron transport chain during respiration, and Fe^{2+} from the reduction forms extracellular fine-grained minerals (*1*). Little is known about changes to the cell and its structure during the reduction of Fe(III) minerals; investigators often use readily soluble organo-Fe(III) complexes (e.g., Fe-citrate), rather than Fe(III) minerals, for metabolic studies on Fe reduction [e.g., (*2*)] because these allow easy isolation of cells without their problematic separation from the granular mineral matrix. Growth on soluble Fe could, however, be quite different from growth on particulate Fe(hydr)oxides, where the substrate is more tenaciously bound. Tracking the fate of the Fe^{2+} produced during dissimilatory reduction of Fe(III) minerals requires the monitoring of changes in the cell during growth as well as in the minerals produced. Such a study can elucidate the pathways of Fe and its toxic analogs (e.g., U, Tc, and Cr) in natural systems, where Fe minerals can be abundant but Fe chelates are rare (*3*).

Cells of *S. putrefaciens* CN32 were grown in a defined medium (*1*, *4*). The initial cell density was 2×10^7 colony-forming units (CFU)/ml, which rapidly decreased to 6×10^6 CFU/ml during the first day and slowly cycled at this level for 2 weeks before declining again. A plateau in CFU/ml was eventually reached, indicating that cells remained active and viable, replacing themselves as others died so that a steady state was reached. This slow growth reflected the relatively poor nutrient conditions relative to traditional batch culture methods.

Hydrous ferric oxide [termed two-line ferrihydrite because of the two broad diffraction lines seen by x-ray diffraction (XRD) (*5*)] was the electron acceptor. These ~50- to 150-nm fine-grained aggregates of ferrihydrite, when added to the medium, immediately adsorbed to the cells (Fig. 1) and were the source of cellular Fe. The Fe concentrations were representative of natural levels commonly found in marine and soil sedimentary environments (*6*, *7*). Significant Fe^{2+} (relative to an uninoculated control) was detected after 1 to 4 days by the ferrozine method (*8*), and Fe^{2+} increased for ~2 weeks before decreasing slowly (Fig. 2). Intracellular fine-grained (30 to 50 nm) granules were first observed by transmission electron microscopy (TEM) 3 to 5 days after inoculation and were never seen before the appearance of Fe^{2+} in the reaction mixture (*9*). By 14 days, the proportion of cells with visible granules had increased to >90% of the population,

Table 1. Electron diffraction data for crystalline intracellular particles formed by *S. putrefaciens* CN32.

Standard magnetite* (nm)	Sample (nm)
0.2967 (30)†	
0.2532 (100)	0.2525 (311)‡
0.2424 (8)	
0.2099 (20)	0.2044 (400)
0.1715 (10)	0.1780 (422)
0.1616 (30)	0.1570 (511)
0.1485 (40)	0.1506 (440)
0.1419 (2)	
0.1328 (4)	
0.1281 (10)	0.1301 (533)
0.1266 (4)	
0.1212 (2)	
0.1122 (4)	
0.1093 (12)	0.1040 (731)

*ASTM card 19-629. †Denotes XRD intensity. ‡Denotes *hkl* values.

Department of Microbiology, College of Biological Science, University of Guelph, Guelph, Ontario N1G 2W1, Canada.

*To whom correspondence should be addressed. E-mail: sglasaue@micro.uoguelph.ca